

Penta-coordinated aluminum species: Anchoring Au single atoms for photocatalytic CO₂ reduction

Shaoqiang Li^a, Yi-lei Li^a, Hui-min Bai^a, Dong-ying Zhou^a, Ying Liu^{a,*}, Rui-hong Liu^a, Bao-hang Han^b, Xinying Liu^c, Fa-tang Li^{a,*}

^a Hebei Key Laboratory of Photoelectric Control on Surface and Interface, College of Science, Hebei University of Science and Technology, Shijiazhuang 050018, China

^b CAS Key Laboratory of Nanosystem and Hierarchical Fabrication, CAS Center for Excellence in Nanoscience, National Center for Nanoscience and Technology, Beijing 100190, China

^c Institute for Catalysis and Energy Solutions, University of South Africa (UNISA), Florida Science Campus, Private Bag X6, Johannesburg 1710, South Africa



ARTICLE INFO

Keywords:

Photocatalytic CO₂ reduction
Amorphous Al₂O₃
Penta-coordinated aluminum species
O vacancy
Au single atom

ABSTRACT

Searching substrate materials having inherent photocatalytic activity and interaction with single atoms remains challenge. Herein, amorphous Al₂O₃ containing penta-coordinated aluminum (Al^V) species is synthesized using the solvothermal method and the Au single atom is anchored by Al^V via the self-reduction strategy. The Al-O bond energy is weakened by introducing amorphous components, which benefits the release of oxygen atoms and the resultant change of Al coordination environment to a Al^V species. The electron transfer between Al^V and Au stabilizes the Au single atom. The introduction of the Au single atom occupying the position of O vacancy and anchored by Al^V strengthened the chemical absorption abilities for CO₂, lowered the energy barrier of CO generation and promoted the charge separation efficiency. The CO generation rate of the Au single atom anchored obtains extraordinary promotion in comparison with pristine Al₂O₃, resulting in an approximately 6-fold enhancement and 98% product CO selectivity.

1. Introduction

The excessive use of fuels has led to severe environmental issues, such as excessive emission of greenhouse gases [1–3]. Carbon dioxide (CO₂), one of the most representative greenhouse gases, has attracted attention due to photocatalytic CO₂ conversion technology which utilizes sunlight as a source of energy [4,5]. Therefore, the design of a photocatalyst with a rational structure is essential to promote performance and selectivity. A large number of reports show that noble metals have been introduced into photocatalysts to promote the activation and further transformation of CO₂ molecules [6–9]. Since Zhang proposed the concept of Single Atom Catalysts (SACs) [10], the research and application of noble SACs have been developing rapidly owing to maximized atomic utilization, excellent activity and selectivity.

In recent years, the choice of substrate materials embedding a single atom has become increasingly diverse, from metal oxides [11] to metal-organic frameworks (MOFs) [12] and carbon-based materials (e.g., graphene [13], carbon nitride [14]). To design high catalytic activity photocatalysts, embedding single-atom metals into metal-based

substrates, which are typically semiconductors, would be an ideal choice by reason of their distinctive characteristics such as their light absorption abilities, redox properties, and plentiful surface binding sites [15]. Moreover, the preparation process of some non-metal-based substrates is complicated and time-consuming, leading to large-scale application and industrialization being further from reality. Therefore, designing cost-effective and efficient metal-based catalysts for anchoring a single atom is of great practical significance.

Al₂O₃, one of the most representative metal oxides, is well known for its characteristics of chemical stability, good earth abundance, cost effectiveness and widespread application as a co-catalyst or substrate [16,17]. Al₂O₃-based photocatalysts have many applications in the field of photocatalysis. In 2012, we found mixed amorphous and crystalline Al₂O₃ exhibited photocatalytic ability under UV-light irradiation and defects in the amorphous components favor the transport of electrons [16]. Subsequently Ismail et al. have demonstrated that the addition of amorphous Al₂O₃ at low contents onto TiO₂ particles led to the synergistic effect and hence increased the separation efficiency of charge carriers [18]. Pathania et al. synthesized Al₂O₃ nanoparticles for

* Corresponding authors.

E-mail addresses: qixiaosong1028@163.com (Y. Liu), lifatang@126.com (F.-t. Li).

photocatalytic degradation of malachite green (MG) dye and found two processes: adsorption followed by photocatalysis; coupled adsorption and photocatalysis. The coupled process exhibited a higher photo-degradation efficiency (45%) compared to adsorption followed by photocatalysis (32%) [19]. Besides, applying Al_2O_3 to photocatalytic CO_2 reduction can be regarded as a good choice. The characteristic of large specific surface area in Al_2O_3 can be combined with defect engineering strategies to make it abundant in active sites. Such as the oxygen vacancy strategy, the constructed oxygen vacancy, as a Lewis acidic site [20], acts to interact with the CO_2 molecules. Recently, our group reported the construction of oxygen vacancies in Al_2O_3 by the elongation of its Al-O bonds [21]. Al_2O_3 containing oxygen vacancy not only obtains a narrower band gap and can absorb ultraviolet light, but also promotes the adsorption and activation of CO_2 molecules, which enables Al_2O_3 to be used as an independent photocatalyst in this reaction.

However, there are tough challenges in Al_2O_3 embedding monatomic noble metals as the electron transfer between weakly reducible Al ions and noble metal atoms are difficult to implement. For example, Zhang's group showed that Al_2O_3 can lead to the agglomeration of Pt nanoparticles in Al_2O_3 due to the weak Pt-O interaction on the surface [22]. Exhilaratingly, Kwak et al. successfully loaded a Pt single atom onto $\gamma\text{-Al}_2\text{O}_3$ and confirmed that the pentahedrally coordinated Al (Al^{V}) site on $\gamma\text{-Al}_2\text{O}_3$ was the critical factor for the formation of a Pt single atom for the first time [23]. Subsequently, Cong's group loaded atomically dispersed Ru molecules on the unsaturated Al^{V} site [24]. Zhang's group fixed a Pt single atom on the abundant Al^{V} sites of mesoporous Al_2O_3 [25]. The methods mentioned to construct Al^{V} sites include evaporation-induced self-assembly [24,25], and flame synthesis [26], but they are obviously far from industrialization.

Taking all aspects into consideration, we exploit a facile method to design amorphous Al_2O_3 containing pentahedrally coordinated aluminum species and a synthetized Au single atom anchored by Al^{V} sites using the self-reduction strategy. By introducing amorphous components and adding a reducing reagent, the Al-O intermolecular forces become weaker and the O atoms are easier to release. In parallel, the Al coordination environment changed from Al^{IV} and Al^{VI} in the regular arrangement coordination environment to the production of an Al^{V} coordination environment containing amorphous components. The NMR & ESR results display the peak signal decreased after anchoring the Au single atom, meaning that Au atoms occupying the position of O vacancy are anchored at the Al^{V} sites. This work proposes the facile synthesis of Al^{V} species for the first time, and reveals the anchoring mechanism of the Au single atom, which provides eventful reference for unsaturated coordination defect and design of the photocatalyst anchoring single atom.

2. Experimental

None of the chemicals were further purified before the experiment. Aluminum nitrate nonahydrate ($\text{Al}(\text{NO}_3)_3 \cdot 9 \text{ H}_2\text{O}$, analytical grade), Urea ($\text{CO}(\text{NH}_2)_2$, analytical grade), and Diethylamine hydrochloride ($\text{C}_4\text{H}_{11}\text{N}\cdot\text{HCl}$, analytical grade) were bought from Aladdin. 1,3,5-benzenetricarboxylic acid (BTC, analytical grade), N, N-dimethylformamide (DMF, analytical grade), ethylene glycol ($(\text{CH}_2\text{OH})_2$, analytical grade) and Hydrogen tetrachloroaurate (III) trihydrate ($\text{HAuCl}_4 \cdot 3 \text{ H}_2\text{O}$, 47.5%) were all obtained from Innochem.

2.1. Preparation of Al-M

In typical synthetic procedure, the precursor was prepared using the solvothermal method [27]. 5 mmol BTC, 10 mmol $\text{Al}(\text{NO}_3)_3 \cdot 9 \text{ H}_2\text{O}$ were dissolved in 60 mL mixture solution of 50 mL DMF/10 mL deionized water. Then the extra 15 mL ethylene glycol was added in the system. Then the mixed solution was transferred to a Teflon-lined autoclave. The reaction system was maintained for 24 h at 160 °C. The crystallization product was washed several times with deionized water, then

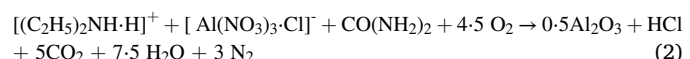
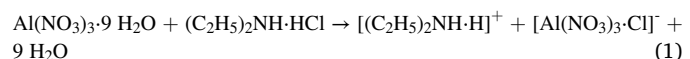
subsequently washed one time with methanol before being placed in an oven overnight at 80 °C under vacuum. The dried sample was calcinated at a heating rate of 2 °C/min to 500 °C to remove carbon impurities. Then the obtained Al_2O_3 containing Al^{V} species was used as a masterplate for anchoring a single atom and was named Al-M.

2.2. Preparation of Al-Au-0.5 and counterparts

500 mg Al-M and 30 mL alcohol were mixed and stirred for 10 min. For 0.5 wt% Au loaded sample, 0.2 mL HAuCl_4 (25 mg/mL) solution was added to the mixed solution and stirred for 5 h. Then the mixture was centrifuged several times with ethanol and dried in an oven overnight at 80 °C under vacuum. The final product was named Al-Au-0.5.

The synthesis procedure of other counterparts was the same as that of Al-Au-0.5, except that different amounts of HAuCl_4 solution were added. For 0.25 wt%, 0.75 wt% and 1 wt% Au loaded samples, 0.1, 0.3, 0.4 mL HAuCl_4 solution were added to the corresponding mixed solution. They were labeled Al-Au-0.25, Al-Au-0.75 and Al-Au-1, respectively.

The synthesis steps of Al_2O_3 containing only O defects but not Al^{V} species are as follows via the ionic liquid self-combustion method developed by our group [28]: 5.02 g $\text{Al}(\text{NO}_3)_3 \cdot 9 \text{ H}_2\text{O}$, 2.2 g $\text{C}_4\text{H}_{11}\text{N}\cdot\text{HCl}$, 3.6 g $\text{CO}(\text{NH}_2)_2$ were mixed and then heated on the preheated electric furnace. In the reducing atmosphere, the mixture melted and underwent spontaneous combustion to form the final product, which was further maintained in a muff furnace at 450 °C for 300 min to shed carbon impurities, and was named as Al^{V} free-Al. The formation process of the target product can be evaluated by the following equations:



The synthesis steps of loading Au on Al^{V} free-Al are similar to the procedure of Al-Au-0.5, which is labelled Al^{V} free-Al-Au-0.5.

2.3. Characterization

The crystal phases and composition of catalysts were implemented on an X-ray diffractometer (Rigaku D/MAX 2500). The morphology of the catalysts was observed on JEOL JSM-7500 scanning electron microscope (SEM). A high-resolution transmission electron microscope (TEM) (FEI Tecnai G2 f20 S-TWIN) was characterized for the microscopic morphology of the catalysts. High Angle Angular Dark Field-Scanning Transmission Electron Microscopy (HAADF-STEM) can provide atomic level resolution. In order to determine the structure of the monoatomic catalyst, it was characterized in Thermo Fisher FEI Thermos Z. ASPA-2020 was used for the Brunauer-Emmett-Teller (BET) method. The optical absorption property can be analyzed by UV-Vis diffuse reflectance spectra (DRS) on the Thermo Fisher Scientific Evolution 200 spectrophotometer. Photoluminescence spectra (PL) of the catalyst were measured by F-4600 fluorescence spectrophotometer from Hitachi, Japan. The CO_2 temperature-programmed desorption analysis (CO_2 -TPD) was obtained using the Beijing Biotech PCA-1000 chemical adsorption instrument. The electron spin resonance (ESR) test was detected on the JES FA200 ESR spectrometer. X-ray photoelectron spectroscopy (XPS) is used to detect the sample's chemical state change on a Thermo Fisher Scientific K-Alpha spectrometer using an Al $\text{K}\alpha$ source. ^{27}Al Nuclear magnetic resonance (NMR) was selected to analyze the coordination and chemical shift changes of aluminum in the prepared catalyst on the JNM-ECZ600R Spectrometer (JEOL RESONANCE Inc., Japan). To detect the intermediates in the reaction process and photocatalytic mechanism, in-situ Fourier-transform infrared (FTIR) spectroscopies were performed on a Bruker INVENIO spectrometer (Germany). The electrochemical properties were implemented on an electro-chemical analyzer CHI660E (Shanghai, China). The

electrochemical tests were conducted using a standard system containing three electrodes. The counter electrode and reference electrode were the platinum electrode and the saturated Ag/AgCl electrode, respectively. The preparation of the working electrode was as follows: 50 mg of catalyst and 10 mg of polyethylene glycol (PEG) were ground and dispersed in 0.3 mL of absolute ethanol, and the mixed solution was evenly coated on the conductive surface of clean indium tin oxide conductive glass (ITO) with a fixed area of about 1 cm².

Details of characterizing the solid phase with X-ray absorption fine structure (XAFS) analyses: Au L-edge analysis was performed with Si (111) crystal monochromators at the BL11B beamlines at the Shanghai Synchrotron Radiation Facility (SSRF) (Shanghai, China). Before analysis at the beamline, samples were pressed into thin sheets with 1 cm in diameter and sealed using Kapton tape film. The XAFS spectra were recorded at room temperature using a 4-channel Silicon Drift Detector (SDD) Bruker 5040. Au L-edge extended X-ray absorption fine structure (EXAFS) spectra were recorded in transmission mode. Negligible changes in the line-shape and peak position of Au L-edge XANES spectra were observed between two scans taken for a specific sample. The XAFS spectra of these standard samples (Au foil) were recorded in transmission mode. The spectra were processed and analyzed by the software codes, Athena and Artemis.

2.4. Photocatalytic activity evaluation

Photocatalytic CO₂ reduction is employed to evaluate the activity. The photocatalytic performance was carried out in an offline stainless-steel reactor. A 300 W xenon lamp for simulating sunlight is the light source. First of all, 3 mg photocatalyst was evenly added on a plate with a bottom area of 1.45 cm². Later, 2.5 mL H₂O was placed at the base of the stainless-steel reactor. Subsequently, the quartz plate coated with the photocatalyst was put on the quartz container containing water. The above-mentioned reaction system was evacuated by a vacuum pump. After that, highly pure CO₂ gas was injected into the reactor to ensure normal pressure. The light source illuminated the stainless-steel reactor from the top. The system of constant temperature circulating water was adopted to ensure that the reaction temperature was 40 °C. The product was detected on a GC9560 gas chromatography. 1 mL of the gas mixture was injected into the gas chromatography using a syringe every 2 h for qualitative analysis.

2.5. DFT calculation details

DFT calculations were performed using the Vienna ab initio Software Package (VASP) [29,30]. Vander Waals interactions were accounted for using the DFT-D3 method [31]. The generalized gradient approximation (GGA) with the Perdew, Burke, and Ernzerh (PBE) functional was adopted to describe the electron exchange-correlation interaction [32, 33]. Electron wave functions were expanded in plane waves with a kinetic energy cutoff of 550 eV. The convergence criterion for the electronic self-consistent iteration and force was set to 10⁻⁵ eV and 0.03 eV/Å, respectively. A vacuum layer of 20 Å was introduced to avoid the interactions between periodic images. For the amorphous Al₂O₃ structure, a supercell with 254 atoms (77 Al atoms and 177 O atoms) was used and the O²⁻ vacancies were generated by deleting an O atom in between the four-coordinate (AlO₄) and five-coordinate (AlO₅) Al site in order to create a gold atom anchored site. The Monkhorst-Pack [34] grids with 1 × 1 × 1 k-point grid were used in all adsorption models. The valence states were 2 s²2p⁴ for O with 6 valence electrons, 3 s²3p¹ for Al with 3 valence electrons, and 5d¹⁰6 s¹ states for Au with 11 valence electrons.

The formation energy of Au located on O vacancy site was calculated using the following formula:



$E_{\text{form}} = E(\text{AuAl}_2\text{O}_{3-x}) + E(1/2 \text{O}_2) - [E(\text{Al}_2\text{O}_3) - E(\text{Au})]$, where the $E(\text{AuAl}_2\text{O}_{3-x})$ and $E(\text{Al}_2\text{O}_3)$ correspond to the total energy of the $\text{AuAl}_2\text{O}_{3-x}$ and amorphous Al_2O_3 (100) surface. The $E(\text{Au})$ comes from the energy of the Au unit cell.

The Gibbs free energies were calculated as $\Delta G = \Delta E_{\text{SCF}} + \Delta ZPE - T\Delta S + CpdT$, where the ΔE_{SCF} is the electronic SCF energies from DFT, ΔZPE is the zero-point energy and $T\Delta S$ is the entropy correct.

3. Results and discussion

3.1. Structural characteristic of Al-Au-0.5

Fig. 1a shows the preparation process of the catalyst. More synthetic details are in experimental section. The peaks of 31.9°, 37.6°, 39.4°, 45.8°, 60.9°, 67° and 84.8° in Al_2O_3 calcinated at 800 °C (Al-800 °C) match well with a standard card (JCPDS NO.10-0425), hence proving the successful preparation of γ - Al_2O_3 catalysts in Fig. S1 [21]. It is comprehensively agreed that the photocatalytic performances in Al_2O_3 depend on the introduction of amorphous components [21]. The Al_2O_3 photocatalyst calcinated at 500 °C (Al-M) is selected as the appropriate substrate to anchor the single atom owing to purity and amorphous degree. Fig. S2 shows morphology characteristics of as-synthesized catalysts by XRD. Obviously, the peaks of all samples rarely change after loading the Au element, indicating no existence of Au nanoparticles [8]. Moreover, compared with Al-M (Fig. S3), SEM images of Al-Au-0.5 shown in Fig. 1b demonstrate that it maintains the original hexagonal structure. Meanwhile, no lattice fringes of Au were observed in the TEM & HRTEM image results (Fig. 1c&d), indicating that the Au element exists in Al_2O_3 at a smaller size. To further investigate the distribution of Au species, atomic-resolution high-angle-annular-darkfield scanning transmission electron microscopy (HAADF-STEM) was implemented (Fig. 1e). There is no doubt that isolated bright dots (highlighted by yellow circles) are recognized as individual Au atoms, which illustrates the atomic dispersion of Au species as anchored on the Al-M. Meanwhile, elemental mappings of Al-Au-0.5 in Fig. 1j prove that the three elements (Au, Al, O) are distributed evenly. Then, inductively coupled plasma optical emission spectroscopy (ICP-OES) was measured for the realistic loaded Au content for subsequent analysis about fine structure and Au coordination environment (Table S1). The results show that the realistic content of the loaded Au is 0.34 wt%, which is slightly less than the theoretical value of 0.47 wt%. It is speculated that there is inevitable loss during centrifugation of the preparation of Al-Au-0.5. Fig. 1f&g display the Au L₃ edge X-ray absorption near edge structure (XANES) spectra and the extended X-ray absorption fine structure (EXAFS) measurements for investigating the chemical states and coordination environment of Au atoms. It can be seen that the valence state of Au species in Al-Au-0.5 is the oxidation state, in comparison with Au foil in Fig. 1f. According to the enlarged image inserted in Fig. 1f, compared with AuCl_3 , the difference of absorption edge energy between them is not significant, indicating that the average oxidation valence state of Au in the sample is close to + 3 valence [35]. Furthermore, there are Al-O and Al-Au contributions in the first shell with no Au-Au contribution (Fig. 1g, Fig. S4), which unambiguously affirms no metallic Au nanoparticles or clusters, consistent with the HAADF-STEM result. This judgment was also supported by wavelet transformation (WT) measurement of Au L₃ edge EXAFS oscillation in Fig. 1h&i. Al-Au-0.5 manifested two intensity maxima at wave vectors k of 6.6 Å⁻¹ and 8.5 Å⁻¹, attributed to Al-O and Al-Au, respectively. In brief, Au single atoms are successfully loaded on Al-Au-0.5.

To investigate whether an Au single atom is anchored on the Al^V site, ²⁷Al nuclear magnetic resonance (NMR) spectroscopy was performed. In Fig. 2a, the spectrum exhibits three characteristic peaks, centered at 4.53, 35.25, and 69.58 parts per million (ppm) chemical shifts in Al-M. The two characteristic ²⁷Al NMR peaks featured at 4.53 and 69.58 ppm were contributed to Al³⁺ species in octahedral (Al-Octa, Al^{VI}) and tetrahedral (Al-Tetra, Al^{IV}) coordination, respectively. The NMR peak at

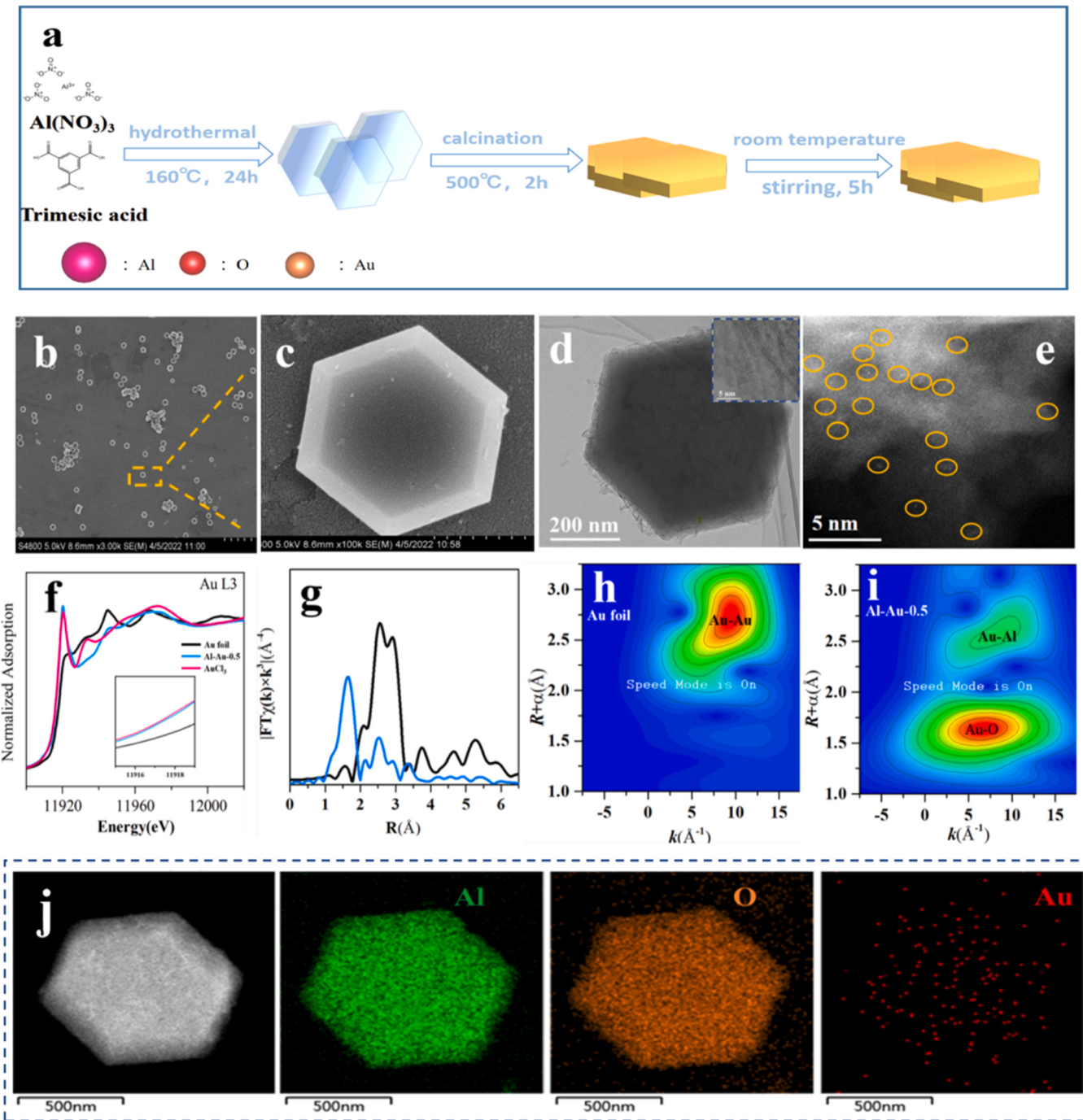


Fig. 1. (a) Schematic illustration of the preparation process of Al-Au-0.5. (b)-(d) The SEM images, TEM images and HRTEM (inset) images of Al-Au-0.5. (e) HAADF-STEM image of Al-Au-0.5. (f) XAFS analysis: Au L₃ XANES spectra. (g) Corresponding k^1 -weighted Fourier transform (FT) EXAFS spectra of the Al-Au-0.5 and the Au foil. (h) & (i) Wavelet Transform analysis in Au foil and the Al-Au-0.5. (j) Elemental mappings of Al-Au-0.5.

35.25 ppm chemical shift was assigned to Al^{3+} species in pentahedral (Al-Penta, Al^{V}) coordination [24,36,37]. Moreover, it should be noted that loading Au on to Al-M results in a decrease in the number of Al^{V} , as demonstrated by the drop of the Al-Penta's NMR peak intensity. Accordingly, the Al-Octa's NMR peak intensity has a large raise after loading Au onto Al-M, which represents the conversion between Al^{V} and Al^{VI} sites [38]. Conclusively, it is evidenced that single Au atoms are anchored by Al^{V} sites through oxygen bridges to saturate the conversion (penta-to octahedral) coordinatively.

To further determine the existence of oxygen defects in the sample, the electron spin resonance (ESR) test was performed. The results in

Fig. 2b manifest signals of $g = 2.003$, which corresponds to oxygen vacancies (OVs) [39]. Equally, it can be seen that the OV signal displays the same tendency as NMR peak intensity after loading Au, explained as Au single atoms having occupied the oxygen vacancies. Therefore, it is speculated that Au single atoms occupied the position of OVs and were anchored by Al^{V} sites. Subsequently, further exploration was conducted on the formation and anchoring mechanisms of Al^{V} sites using density functional theory (DFT) calculations.

Firstly, the formation mechanism of Al^{V} species should be explored; hence, the Crystal Orbital Hamilton Population (COHP) was calculated to investigate the difference in the bonding/antibonding property of

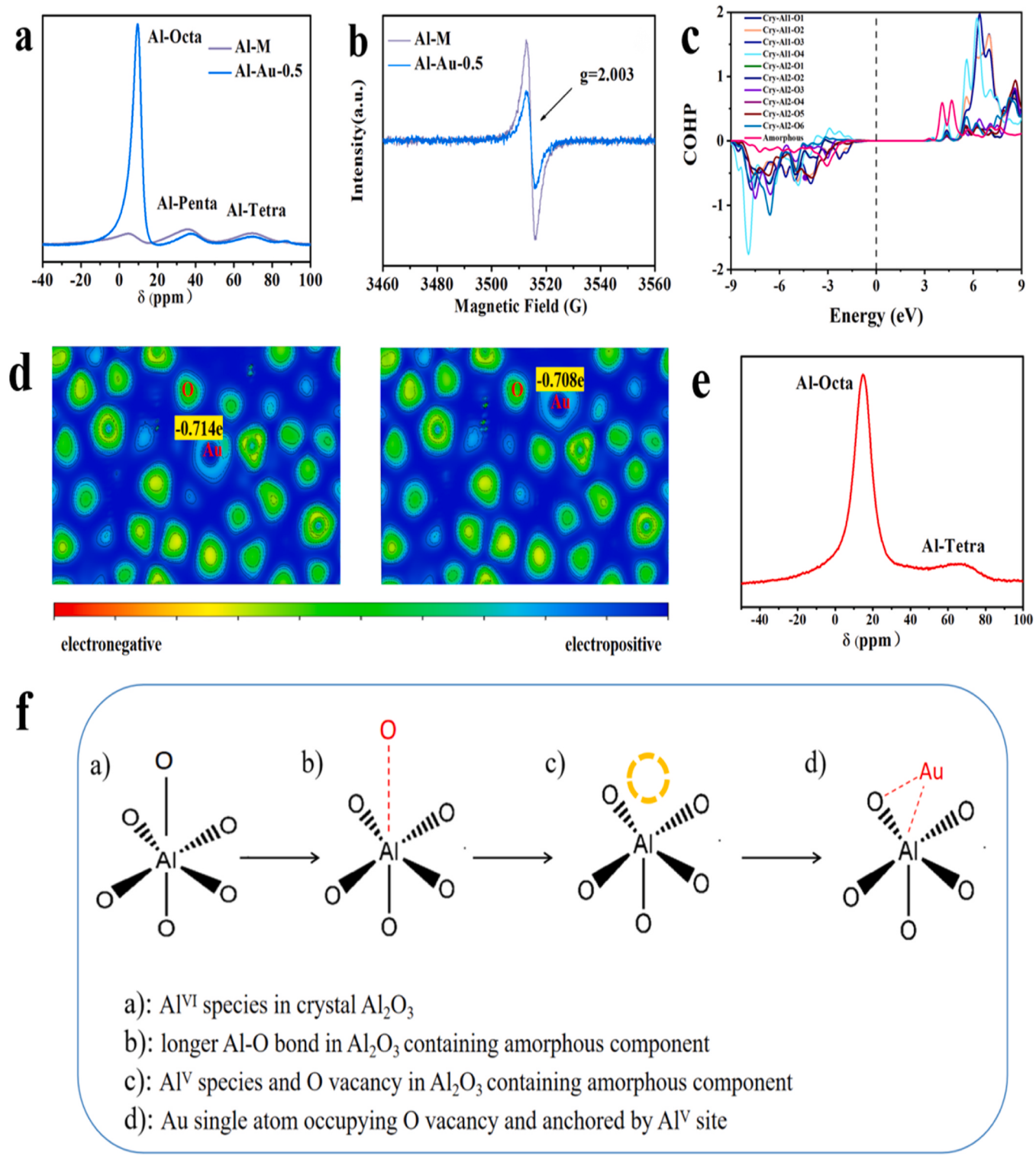


Fig. 2. (a) ^{27}Al NMR spectroscopy and (b) The ESR spectra of Al-M & Al-Au-0.5. (c) COHP analysis of crystal Al_2O_3 and Al_2O_3 containing amorphous components. (d) Corresponding electron localization function of two structural models in Al-Au-0.5. (e) The NMR spectra of Al^{V} -free-Al. (f) The illustration diagram of an Au single atom anchored to Al^{V} sites.

crystal Al_2O_3 and Al_2O_3 containing amorphous components (Fig. 2c, Table S3). The integrated COHP (ICOHP) value of the Al-O bond suggests the Al-O bond stability [40]. The lower value in Al_2O_3 containing amorphous components indicates the instability of the Al-O bond. It can be concluded that by inducing amorphous components, the stability of the Al-O bonds is disrupted, leading to lower oxygen vacancy formation energy [21] and the formation of Al^{V} species. Afterwards, the DFT

results in Fig. S5 shows the two pathways of Au anchored in Al-Au-0.5: one is the single Au atom occupying the O vacancy which is anchored at a Al^{V} site and a Al^{IV} site, and the other occupying the O vacancy is anchored at one Al^{V} site and two Al^{IV} sites. There is no obvious difference between their single atom formation energies (E_{form}), proving that Al^{V} sites play a vital role in anchoring an Au single atom. Furthermore, as shown in Fig. 2d, the electron localization function (ELF) of two

structural models in Al-Au-0.5 manifests that a positive charge surrounding the Au single atom indicates that the electron was transferred to the Al and O connected to it. Based on the above results, the structural characteristics of Al-M with both Al^{V} species and oxygen vacancies synergistically stabilize the Au single atom.

Furthermore, in order to further emphasize the anchoring effect of Al^{V} from the perspective of the experimental results, we synthetized one type of Al_2O_3 material, and named it $\text{Al}^{\text{V}}\text{free-Al}$; it contains O vacancy only and does not contain an Al^{V} site. $\text{Al}^{\text{V}}\text{free-Al}$ was obtained via the ionic liquid self-combustion method developed by our group [28]. The basic principle is that the raw materials gradually melt to form an ionic liquid, and then undergo spontaneous combustion reaction in a reducing atmosphere to form alumina rich in oxygen vacancies [28]. Due to violent reaction and the reducing atmosphere, octa-coordinated aluminum may tend to lose two oxygen atoms simultaneously and form tetra-coordinated aluminum instead of penta-coordinated aluminum.

The DRS spectrum was used to analyze the light absorption of the counterpart. As shown in Fig. S6, compared with Al-M containing more amorphous components, the $\text{Al}^{\text{V}}\text{free-Al}$ exhibits weaker light absorption ability, which is consistent with our previous conclusion. Then the $\text{Al}^{\text{V}}\text{free-Al-Au-0.5}$ was attained in the same method as Al-Au-0.5 except that the substrate is $\text{Al}^{\text{V}}\text{free-Al}$. The XRD patterns of $\text{Al}^{\text{V}}\text{free-Al}$ in Fig. S7a show that the good match with the standard card (JCPDS No. 01-083-2080), proving the successful preparation of the Al_2O_3 material. To confirm the defect types and Al coordination environment, ESR and NMR tests are obtained in $\text{Al}^{\text{V}}\text{free-Al}$. The results shown in Fig. 2e & Fig. S8 demonstrate that there are only O vacancies with no existence of Al^{V} species in $\text{Al}^{\text{V}}\text{free-Al}$. Meanwhile, the existence form of Au should be determined after introducing Au into $\text{Al}^{\text{V}}\text{free-Al}$. At first, $\text{Al}^{\text{V}}\text{free-Al-Au-0.5}$ does not show any Au diffraction peak in XRD in Fig. S7b. Then, compared with $\text{Al}^{\text{V}}\text{free-Al}$, the drop of peak in the ESR results means that Au elements occupied the position of O vacancies. To explore the existence form of the Au element, TEM was obtained in $\text{Al}^{\text{V}}\text{free-Al-Au-0.5}$. In Fig. S7c&d, it can be seen that the crystal lattice stripes with width of 0.23 nm correspond to the (111) planes of the Au metal [41]. Hence this confirms the anchoring effect of Al^{V} species from an experimental perspective. Moreover, XPS analysis is applied to determine the chemical composition and chemical state of the counterpart. The XPS analysis diagrams of $\text{Al}^{\text{V}}\text{free-Al-Au-0.5}$ photocatalysts are shown in Fig. S9, which displays the signal of Au and indicates the effective introduction of Au element [42]. In order to analyze the true content of introduced Au element, ICP-OES test was also conducted. The result in Table S4 shows that the amount of Au introduced is not the only factor that determines whether Au element exists as single atom or cluster, but is also related to defects on the Al_2O_3 surface. In addition, the aluminum coordination form of commercial Al_2O_3 is also determined by NMR tests in Fig. S10, which shows the absence of penta-coordinated aluminum species. Based on the above theoretical analysis and experimental results, a conclusion can be drawn: Al_2O_3 containing only O vacancy but not Al^{V} species cannot efficiently anchor single atoms. Referencing to Zhang et al.'s work about nature of Penta-Coordinated Al revealed by ultra-highfield solid-state NMR [43], the illustration diagram of an Au single atom anchored by Al^{V} sites is shown in Fig. 2 f.

3.2. Photocatalytic CO_2 reduction performance of Al-Au-0.5

The photocatalytic performances of as-designed samples were evaluated under simulated solar light. It is noteworthy that no sacrificial reagents were used during the whole test, and the proton source is water, which is abundant in nature. As mentioned previously, the photocatalytic performance of pristine Al_2O_3 is associated with its amorphous degree. By altering the calculation temperature, better performance of Al-M was attained, compared with Al-800 °C, which confirms the aforementioned conclusion (Fig. S11a). Moreover, according to the NMR results in Fig. S11b, the content of Al^{V} species in Al-M is more

abundant. Therefore, considering the intrinsic activity of Al_2O_3 and anchoring the Au single atom efficiently, Al-M was selected as a masterplate for loading the Au element. In Fig. 3a, the best photocatalytic performance of as-designed samples is the 0.5 wt% Au loaded sample (denoted as Al-Au-0.5), reaching the CO production rate of 31.7 $\mu\text{mol g}^{-1} \text{h}^{-1}$, approximately 6 times that of Al-M.

As the amount of Au loaded increases, the photocatalytic activity decreases due to the formation of Au clusters [8], which can be proved by HAADF-STEM in Fig. S12. It should be noted that no matter whether the Au single atom is embedded or not, there is only trace CH_4 present and no H_2 generation in the product composition in Fig. S13. CH_4 begins to generate in the third hour of Al-M, while in Al-Au-0.5 it is the fourth hour, indicating that the introduction of Au single atom promotes the conversion of CO_2 to CO. Meanwhile, the product selectivity, the key factors of photocatalytic CO_2 reduction [44], is shown in Fig. S14. It can be seen that as the reaction proceeds, the introduction of Au single atom increases the selectivity of the product CO from 94% to 98%. This reason will also be illustrated in detail with DFT results. Moreover, it is widely known that stability, one of the most substantial factors, plays an essential role as a photocatalyst. To our delight, Al-Au-0.5 demonstrated excellent stability in several recycling reaction tests (Fig. 3b). More importantly, the control experiments were implemented to illustrate a series of issues such as product source. In the situation of no photocatalyst, the almost undetectable product rate indicates that the reaction requires the involvement of a catalyst. In the dark condition, the result strongly proves that the solar light is the driving force. Moreover, to elaborate the carbon source and to avoid dispensable or misleading issues owing to inevitable organic impurities, the blank test was examined, which elucidates clearly that CO is the only reduction product under equivalent conditions (Fig. 3c). Furthermore, Fig. 3d showed the photocatalytic activities of all samples and the photoactivity of Al^{V} -free-Al-Au-0.5 showed a significant decrease compared to before loading Au, due to the aggregation of Au nanoparticles in Fig. S7c&d.

The ability of light response is the most significant characteristic for photocatalysts; hence, the UV-Vis diffuse reflection absorption spectrum was obtained. It should be noticed there is only a slight change in the absorption edges between Al-M and Al-Au-0.5 in Fig. 4a, suggesting that the introduced Au single atom does not alter the absorption edge obviously. Meanwhile, it can be deduced that the ability of light response is not the most crucial aspect of photocatalytic performance at least. The band gap energy (E_g) of photocatalyst could be obtained according to the formula $\alpha(h\nu)=A(h\nu-E_g)^{n/2}$ (Fig. S15a). The Mott-Schottky test was implemented to detect the flat band potential of the prepared samples the positive slope implies the characteristics of its n-type semiconductor. Moreover, the flat band potentials of Al-M and Al-Au-0.5 relative to the Ag/AgCl electrode can also be obtained, which are -1.44 V and -1.39 V, respectively. According to $E_{\text{NHE}} = E_{\text{Ag/AgCl}} + E_{\text{Ag/AgCl}}^{\circ} + 0.059 \text{ pH}$ ($\text{pH} = 6.8$, $E_{\text{Ag/AgCl}}^{\circ} = +0.199 \text{ V}$), where E_{NHE} corresponds to the electrode potential of normal hydrogen electrode at $\text{pH}=0$ and $E_{\text{Ag/AgCl}}^{\circ}$ represents the electrode potential of standard Ag/AgCl electrode, the flat band potentials of Al-M and Al-Au-0.5 relative to hydrogen electrode are -0.84 V and -0.79 V, respectively [45]. Generally, the flat band potential of the n-type semiconductor relative to the hydrogen electrode can be used to represent the conduction band potential [28]. Furthermore, the valence band potential of sample can be calculated by $E_{\text{VB}} = E_{\text{CB}} + E_g$ (E_{VB} and E_{CB} stand for valence band potential and conduction band potential, respectively) [21], so the valence bands of Al-M and Al-Au-0.5 are 2.11 V and 2.07 V, respectively. The obtained band structure diagram is shown in Fig. S15c. In addition, the adsorption capacity of CO_2 molecules is significant for further molecule activation. Therefore, to identify adsorption capacity change, the N_2 adsorption experiments were conducted. As shown in Fig. S16, the specific surface area has decreased after Au single atoms were anchored, from 9.64 m^2/g to 7.07 m^2/g , meaning the efficient introduction of the Au element. Then the CO_2 adsorption isotherms experiment result shows the similar adsorption capacity of Al-Au-0.5 compared with Al-M (Fig. S17).

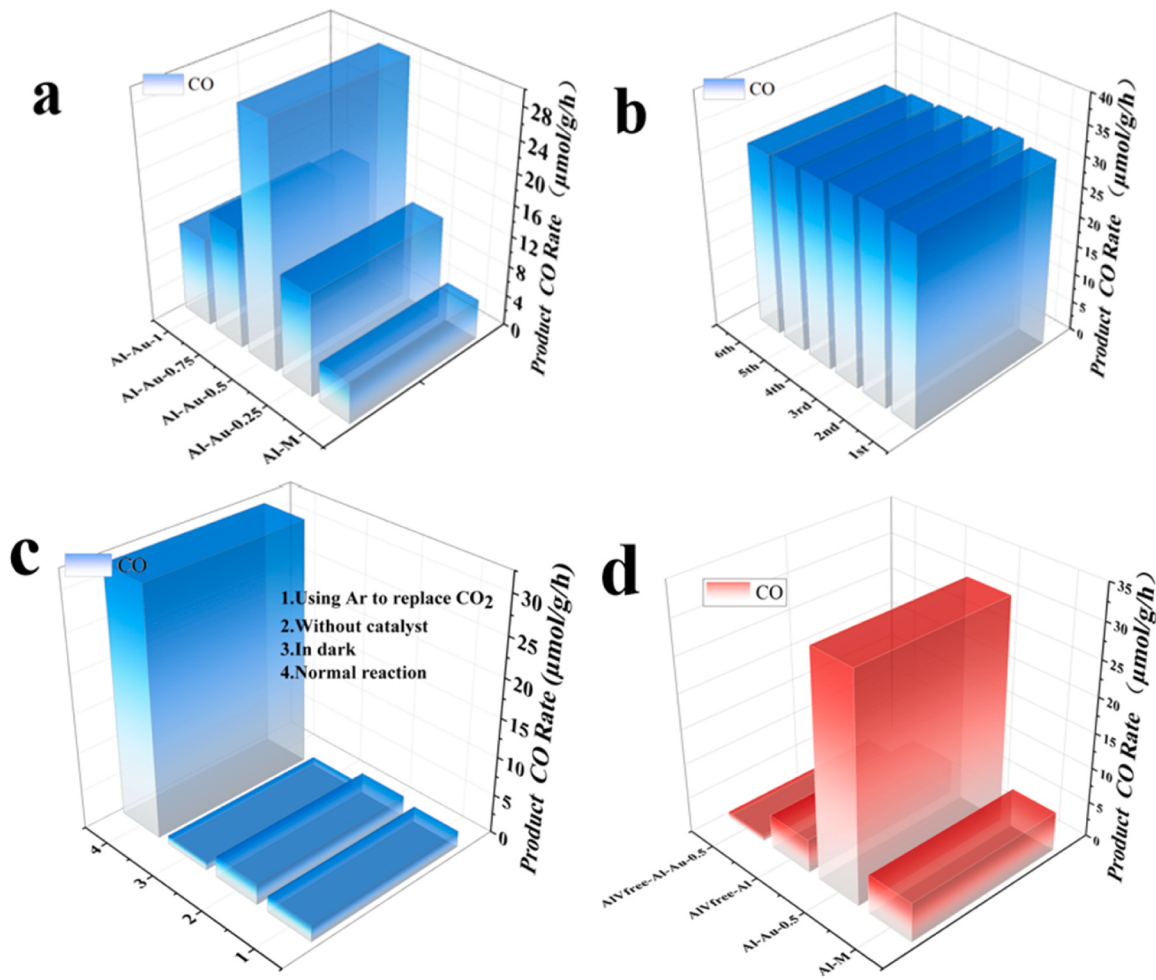


Fig. 3. (a) Photocatalytic CO_2 reduction performances of different loading Au content. (b) Photocatalytic CO_2 reduction performance recycling of Al-Au-0.5. (c) Control experiment in various conditions. (d) Photocatalytic activities of all samples.

Afterwards, the temperature programmed desorption of CO_2 (CO_2 -TPD) was performed for estimating interaction between the catalyst and CO_2 molecules. The desorption peaks in the low and high temperature region represent physical adsorption and chemical adsorption respectively [46]. As can be seen from Fig. 4b, compared with Al-M, commercial Al_2O_3 features stronger physical adsorption of CO_2 molecules as its large specific surface area. In the range of chemical adsorption, Al-M with oxygen vacancy showed strengthened ability to bind with CO_2 molecules. And the commercial Al_2O_3 without surface defects has little effect on the chemisorption area. After the introduction of Au single atom, the catalyst for the physical and chemical adsorption capacity of CO_2 molecules is greatly enhanced, which shows the positive effect of the introduced Au single atom on the adsorption and activation of CO_2 molecules. That is, Al-Au-0.5 features the enhanced ability to sensitize more CO_2 molecules for the further transformation process. In conclusion, the anchored Au single atoms enhanced the ability of CO_2 molecule activation while barely changing the light response.

Normally, the photocatalytic activity is related to photoelectrons, which involves the efficient separation of photogenerated carriers. In view of this, the transient photocurrent response, electrochemical impedance and photoluminescence (PL) spectra are illustrated to clarify the photocarriers' dynamics. Fig. 4c shows that Al-Au-0.5 with an anchored Au single atom obtained the strongest photocurrent response among its counterparts. In Fig. 4d, the most aduncous arc radius in Al-Au-0.5 features the characteristic of minimum transmission resistance, which is advantageous for photocarrier separation [47]. Furthermore, the PL test was used to inspect the separation efficiency of

photogenerated carriers. Normally, the stronger PL peak represents the worse photocarrier separation, meaning lower photocatalytic activity [48]. In contrast, it is obvious that the PL peak of Al-Au-0.5 becomes stronger compared with Al-M in this research in Fig. 4e. That is because the defect sites can capture induced electrons to become free or binding excitons, leading to an easier PL process [49–51]. Therefore, the defect sites in the amorphous part play a more important role in this case.

3.3. Photocatalytic CO_2 reduction mechanism of Al-Au-0.5

Photogenerated electrons separated from holes will be migrated to the surface of the catalyst under illumination. The following process will take place: the CO_2 molecule is combined with the photocatalyst, as the first priority step, which is not facile due to the thermodynamically stable C=O bond. Afterwards, the active species (CO_2^- , CO_3^{2-} , COO^-) originated from the combination of adsorbed CO_2 and photogenerated electrons. Then, the active species will be further converted to final products such as CO and CH_4 . To clarify how the reaction occurs in this system, in situ Fourier Transform Infrared Spectrum (FTIR) measurement in Fig. 4f&g was obtained to investigate the intermediates generated in the reaction process. It is indicated that the absorption bands in Al-Au-0.5 become more abundant and intense, in comparison with Al-M. In detail, the peaks of 1770, 1696, 1456, 1412 cm^{-1} are attributed to carboxyl (COOH), absorbed CO_2 molecules (CO_2^-), carbonate (CO_3^{2-}), and bicarbonate (HCO_3^-), respectively, which are universal absorption bands in Al-M & Al-Au-0.5 [52–54]. In contrast, the peaks of 1541, 1558 cm^{-1} are found to be ascribed to monodentate carbonate (m-CO_3^{2-}) [55].

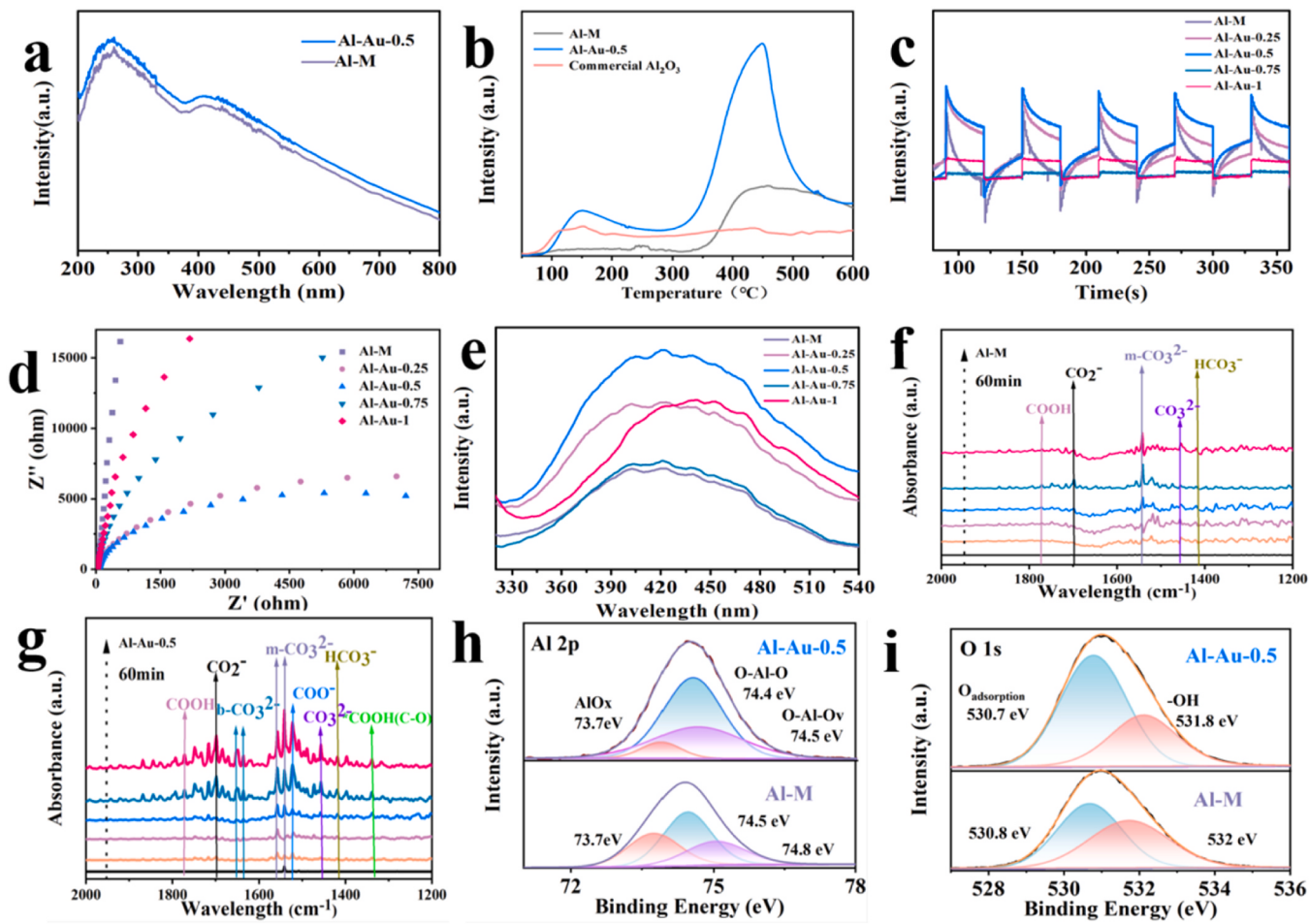


Fig. 4. (a) The DRS spectra of Al-M & Al-Au-0.5. (b) CO_2 -TPD of Al-M & Al-Au-0.5 & Commercial Al_2O_3 . (c) Transient photocurrent response spectrum & (d) EIS spectrum & (e) PL spectra of all samples. The in situ FTIR spectra under simulated solar light illumination : (f) Al-M g Al-Au-0.5. XPS spectra of Al-M & Al-Au-0.5 (h) Al 2p and (i) O 1s.

Meanwhile, the peaks of 1652 , 1636 cm^{-1} are found to be ascribed to bidentate carbonate ($\text{b}-\text{CO}_3^{2-}$) [56]. Besides, the peak at 1332 cm^{-1} is assigned to C-O vibration in absorbed carboxyl (COOH^*) [57]. The enhancement of absorption bands demonstrates that the absorbed CO_2 molecules on Al-Au-0.5 are much more activated in the reaction process. It can be concluded that the abilities of absorption and activation for CO_2 molecules has been strengthened after the intervention of single Au atoms anchored by Al^{V} sites.

To further identify the chemical composition of Al-Au-0.5, X-ray photoelectron spectroscopy (XPS) was implemented to determine the chemical state of the Al-M and Al-Au-0.5 photocatalysts. As shown in Fig. 4h, the Al 2p spectra of Al-M demonstrates that the characteristic peaks at 73.7 eV , 74.5 eV , and 74.8 eV are identified as the signal of AlOx , O-Al-O and O-Al-Ov [28,58], respectively. The O 1s spectra of Al-M (Fig. 4i) demonstrate that the characteristic peaks at 530.8 and 532 eV are identified as the signal of $\text{O}_{\text{adsorption}}$ and surface hydroxyl groups [59], further meaning the success of defective Al_2O_3 preparation. For the Al-Au-0.5 system, binding energy of Al 2p at 73.7 eV , 74.4 eV , and 74.5 eV was found to be ascribed to AlOx , O-Al-O and O-Al-Ov, respectively. Binding energy of O 1s at 530.7 eV , and 531.8 eV was found to be ascribed to $\text{O}_{\text{adsorption}}$ and surface hydroxyl groups [59]. It can be seen that no signal of Au 4f was detected in Al-Au-0.5, attributing to a low amount of Au in the load. Moreover, it should be noted that both the characteristic peaks in the Al 2p and O 1s spectra represent a shift toward low binding energy (0.2 – 0.3 eV) in comparison with the Al-M, indicating that the Al and O element have received the electrons of Au single atoms and the successful introduction of the Au element, which is

consistent with the ELF results.

As demonstrated in Fig. 5a, the possible reaction profiles of photocatalytic CO_2 reduction are simulated by DFT calculations. All the energy barriers on Al-Au-0.5 are lower than that of Al-M, which strongly illustrates the effect of facilitating CO_2 molecules by introducing single Au atoms. Particularly, in the first step in the process ($\text{CO}_2^* + \text{H}^* \rightarrow \text{COOH}^*$), its energy barrier is decreased by 36% relative to that over its counterparts, which suggests that by introducing Au single atoms, the electrons not only promote the activation of CO_2 molecules, but also facilitate their further conversion. Meanwhile, the rate determining step (RDS) was the formation of CO ($\text{CO}^* \rightarrow \text{CO}$) as its highest energy barrier. It should be noted that in Fig. 5b the energy barrier of the essential step for CH_4 conversion ($\text{CO}^* \rightarrow \text{CHO}^*$) is much higher than for the formation of CO, which illustrates that CH_4 evolution might not take place to a great extent [60]. Furthermore, according to Tang et al.'s report, the generation of hydroxyl radicals during photocatalytic processes may be detrimental to methane selectivity [61]. ESR spin capture experiment was performed to disclose active species during reaction process to verify the product selectivity mechanism. In Fig. S18, both Al-M and Al-Au-0.5 show signal peaks of 1:2:2:1 under light conditions, which is the characteristic signal of DMPO-•OH. Obviously the hydroxyl radicals of Al-Au-0.5 is more than Al-M, which illustrates the increase of hydroxyl group also affects the selectivity of the product to some extent [61]. To further prove the product composition possibilities at different temperatures, in situ FTIR measurement at $130 \text{ }^\circ\text{C}$ was obtained, as shown in Fig. S19. Interestingly, the essential active species towards CH_4 ($\text{CHO}^* \& \text{CH}_3\text{O}^*$) were observed, which were non-existent in the in situ

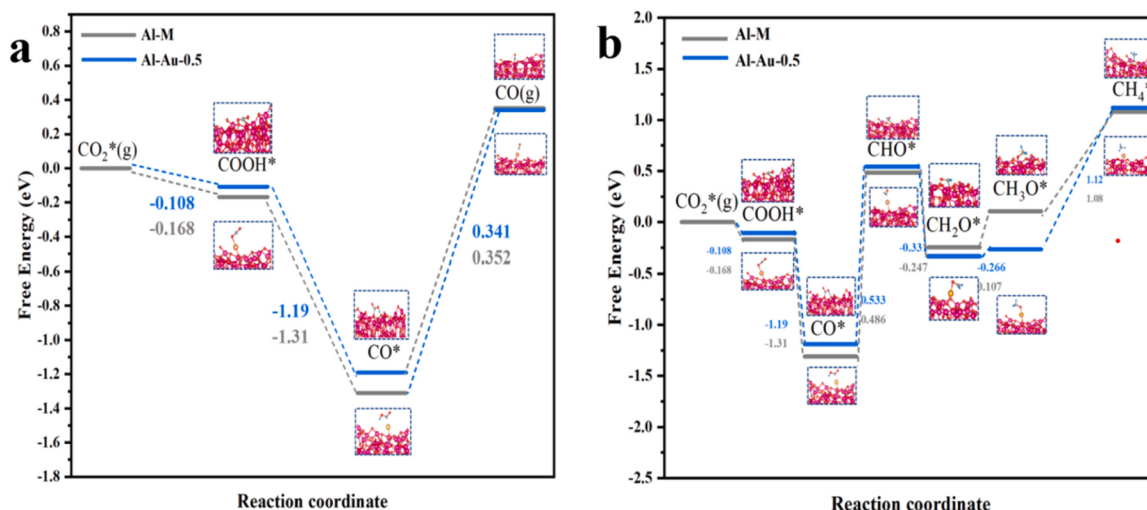


Fig. 5. Energy barriers of different CO₂ photoreduction product over Al-Au-0.5 & Al-M: (a) CO pathway, (b) CH₄ pathway.

FTIR measurement at room temperature. This is consistent with the DFT results. It could not be ignored that there is also almost no CH₄ detected for Al-M, contributing to insufficient photogenerated electrons participating in the subsequent hydrogenation reaction after the formation of CO*. The further CH₄ reaction profile over Al-M demonstrates the same conclusion as Al-Au-0.5, that is, the formation of CH₄ is thermodynamically disadvantageous.

4. Conclusion

By introducing an amorphous component, penta-coordinated Al species in Al_2O_3 was prepared using the solvothermal method. Meanwhile, an Au single atom occupying O vacancy and anchored by penta-coordinated Al species was also successfully designed using the self-reduction strategy. The influence of introducing an Au single atom can be summarized in two ways: On the one hand, an Au single atom greatly strengthened the Al_2O_3 adsorption ability for CO_2 molecules, both physically and chemically, which facilitates the activation of CO_2 molecules. On the other hand, the introduced Au single atoms improve the carrier separation efficiency, leading more photogenerated electrons to participate in the reduction reaction. Meanwhile, Al_2O_3 containing penta-coordinated Al species thermodynamically stabilized the single atom. The synergistic effect between Al_2O_3 and the Au single atom leads to remarkable enhancement and 98% CO selectivity, with approximately 6-fold enhancement of product CO. This research has broadened the application of Al_2O_3 from individual photocatalysts to photocatalysts which can anchor a single atom. Due to the universality of Al_2O_3 , this work also provides a construction route and new reference of unsaturated coordination defect in weakly reducible oxides for efficiently anchoring a single atom.

CRediT authorship contribution statement

Han Bao-Hang: Conceptualization, Methodology, Software. **Liu Rui-hong:** Data curation, Formal analysis. **Li Fatang:** Conceptualization, Funding acquisition, Project administration, Resources, Supervision, Writing – review & editing. **Liu Xinying:** Software, Supervision, Writing – review & editing. **Bai Hui-min:** Data curation, Investigation. **Li Yi-lei:** Formal analysis, Investigation, Methodology. **Liu Ying:** Conceptualization, Supervision. **Zhou Dong-ying:** Data curation, Investigation. **Li Shaoqiang:** Data curation, Formal analysis, Writing – original draft.

Declaration of Competing Interest

The authors declare that they have no known competing financial interests or personal relationships that could have appeared to influence the work reported in this paper.

Data availability

Data will be made available on request.

Acknowledgements

This work is supported by National Key R&D Program of China (2022YFE0101800), National Natural Science Foundation of China (22178084), and Foundation for Innovative Research Groups of the Natural Science Foundation of Hebei Province (no. B2021208005).

Appendix A. Supporting information

Supplementary data associated with this article can be found in the online version at [doi:10.1016/j.apcatb.2024.123703](https://doi.org/10.1016/j.apcatb.2024.123703).

References

- [1] P. Liu, Z. Huang, X. Gao, X. Hong, J. Zhu, G. Wang, Y. Wu, J. Zeng, X. Zheng, Synergy between Palladium single atoms and nanoparticles via hydrogen spillover for enhancing CO₂ photoreduction to CH₄, *Adv. Mater.* 34 (2022) 2200057, <https://doi.org/10.1002/adma.202200057>.
 - [2] X. Ren, M. Gao, Y. Zhang, Z. Zhang, X. Cao, B. Wang, X. Wang, Photocatalytic reduction of CO₂ on BioX: effect of halogen element type and surface oxygen vacancy mediated mechanism, *Appl. Catal. B Environ.* 274 (2020) 119063, <https://doi.org/10.1016/j.apcatb.2020.119063>.
 - [3] X. Cheng, J. Zhang, X. Tan, L. Zheng, D. Tan, L. Liu, G. Chen, Q. Wan, B. Zhang, F. Zhang, Z. Su, B. Han, J. Zhang, Improved photocatalytic performance of metal-organic frameworks for CO₂ conversion by ligand modification, *Chem. Commun.* 56 (2020) 7637–7640, <https://doi.org/10.1039/DCC02707C>.
 - [4] L. Hao, L. Kang, H. Huang, L. Ye, K. Han, S. Yang, H. Yu, M. Batmunkh, Y. Zhang, T. Ma, Surface-halogenation-induced atomic-site activation and local charge separation for superb CO₂ photoreduction, *Adv. Mater.* 31 (2019) 1900546, <https://doi.org/10.1002/adma.201900546>.
 - [5] Y. Li, J. Hao, H. Song, F. Zhang, X. Bai, X. Meng, H. Zhang, S. Wang, Y. Hu, J. Ye, Selective light absorber-assisted single nickel atom catalysts for ambient sunlight-driven CO₂ methanation, *Nat. Commun.* 10 (2019) 2359, <https://doi.org/10.1038/s41467-019-10304-y>.
 - [6] S. Fang, X. Zhu, X. Liu, J. Gu, W. Liu, D. Wang, W. Zhang, Y. Lin, J. Lu, S. Wei, Y. Li, T. Yao, Uncovering near-free platinum single-atom dynamics during electrochemical hydrogen evolution reaction, *Nat. Commun.* 11 (2020) 1029, <https://doi.org/10.1038/s41467-020-14848-2>.
 - [7] N.J. O'Connor, A.S.M. Jonayat, M.J. Janik, T.P. Senftle, Interaction trends between single metal atoms and oxide supports identified with density functional theory

- and statistical learning, *Nat. Catal.* 1 (2018) 531–539, <https://doi.org/10.1038/s41929-018-0094-5>.
- [8] Y. Cao, L. Guo, M. Dan, D.E. Doronkin, C. Han, Z. Rao, Y. Liu, J. Meng, Z. Huang, K. Zheng, P. Chen, F. Dong, Y. Zhou, Modulating electron density of vacancy site by single Au atom for effective CO₂ photoreduction, *Nat. Commun.* 12 (2021) 1675, <https://doi.org/10.1038/s41467-021-21925-7>.
- [9] T.W. van Deelen, C. Hernández Mejía, K.P. de Jong, Control of metal-support interactions in heterogeneous catalysts to enhance activity and selectivity, *Nat. Catal.* 2 (2019) 955–970, <https://doi.org/10.1038/s41929-019-0364-x>.
- [10] B. Qiao, A. Wang, X. Yang, L.F. Allard, Z. Jiang, Y. Cui, J. Liu, J. Li, T. Zhang, Single-atom catalysis of CO oxidation using Pt₁/FeO_x, *Nat. Chem.* 3 (2011) 634–641, <https://doi.org/10.1038/nchem.1095>.
- [11] R. Lang, X. Du, Y. Huang, X. Jiang, Q. Zhang, Y. Guo, K. Liu, B. Qiao, A. Wang, T. Zhang, Single-atom catalysts based on the metal-oxide interaction, *Chem. Rev.* 120 (2020) 11986–12043, <https://doi.org/10.1021/acs.chemrev.0c00797>.
- [12] P. Ji, Y. Song, T. Drake, S.S. Veroneau, Z. Lin, X. Pan, W. Lin, Titanium (III)-oxo clusters in a metal-organic framework support single-site Co(II)-hydride catalysts for arene hydrogenation, *J. Am. Chem. Soc.* 140 (2018) 433–440, <https://doi.org/10.1021/jacs.7b11241>.
- [13] P. Du, K. Hu, J. Lyu, H. Li, X. Lin, G. Xie, X. Liu, Y. Ito, H.J. Qiu, Anchoring Mo single atoms/clusters and N on edge-rich nanoporous holey graphene as bifunctional air electrode in Zn-air batteries, *Appl. Catal. B Environ.* 276 (2020) 119172, <https://doi.org/10.1016/j.apcatb.2020.119172>.
- [14] C. Gao, J. Low, R. Long, T. Kong, J. Zhu, Y. Xiong, Heterogeneous single-atom photocatalysts: fundamentals and applications, *Chem. Rev.* 120 (2020) 12175–12216, <https://doi.org/10.1021/acs.chemrev.9b00840>.
- [15] R. Qin, K. Liu, Q. Wu, N. Zheng, Surface coordination chemistry of atomically dispersed metal catalysts, *Chem. Rev.* 120 (2020) 11810–11899, <https://doi.org/10.1021/acs.chemrev.0c00949>.
- [16] F.T. Li, Y. Zhao, Y.J. Hao, X.J. Wang, R.H. Liu, D.S. Zhao, D.M. Chen, N-doped P25 TiO₂-amorphous Al₂O₃ composites: one-step solution combustion preparation and enhanced visible-light photocatalytic activity, *J. Hazard. Mater.* 239–240 (2012) 118–127, <https://doi.org/10.1016/j.jhazmat.2012.08.016>.
- [17] C. Fauth, A. Lener, A.M. Abdel-Mageed, R.J. Behm, Temporal analysis of products (TAP) reactor study of the dynamics of CO₂ interaction with a Ru/γ-Al₂O₃ supported catalyst, *Appl. Catal. B Environ.* 334 (2023) 122817, <https://doi.org/10.1016/j.apcatb.2023.122817>.
- [18] A.A. Ismail, I. Abdelfattah, M.F. Atitar, L. Robben, H. Bouzid, S.A. Al-Sayari, D. W. Bahnemann, Photocatalytic degradation of imazapyr using mesoporous Al₂O₃-TiO₂ nanocomposites, *Sep. Purif. Technol.* 145 (2015) 147–153, <https://doi.org/10.1016/j.seppur.2015.03.012>.
- [19] D. Pathania, R. Katwal, Harpreet Kaur, Enhanced photocatalytic activity of electrochemically synthesized aluminum oxide nanoparticles, *Int. J. Miner. Metall. Mater.* 23 (2016) 358–371, <https://doi.org/10.1007/s12613-016-1245-9>.
- [20] Y. Zheng, K. Fu, Z. Yu, Y. Su, R. Han, Q. Liu, Oxygen vacancies in a catalyst for VOCs oxidation: synthesis, characterization, and catalytic effects, *J. Mater. Chem. A* 10 (2022) 14171–14186, <https://doi.org/10.1039/D2TA03180A>.
- [21] S.Q. Li, Y. Liu, Y.L. Li, Y.J. Hao, R.H. Liu, L.J. Chen, F.T. Li, Development of γ-Al₂O₃ with oxygen vacancies induced by amorphous structures for photocatalytic reduction of CO₂, *Chem. Commun.* 58 (2022) 11649–11652, <https://doi.org/10.1039/D2CC04546J>.
- [22] R. Lang, W. Xi, J.C. Liu, Y.T. Cui, T. Li, A.F. Lee, F. Chen, Y. Chen, L. Li, L. Li, J. Lin, S. Miao, X. Liu, A.Q. Wang, X. Wang, J. Luo, B. Qiao, J. Li, T. Zhang, Non defect-stabilized thermally stable single-atom catalyst, *Nat. Commun.* 10 (2019) 234, <https://doi.org/10.1038/s41467-018-08136-3>.
- [23] J.H. Kwak, J. Hu, D. Mei, C.W. Yi, D.H. Kim, C.H.F. Peden, L.F. Allard, J. Szanyi, Coordinatively unsaturated Al³⁺ centers as binding sites for active catalyst phases of Platinum on γ-Al₂O₃, *Science* 325 (2009) 1670–1673, <https://doi.org/10.1126/science.1176745>.
- [24] N. Tang, Y. Cong, Q. Shang, C. Wu, G. Xu, X. Wang, Coordinatively unsaturated Al³⁺ sites anchored subnanometric ruthenium catalyst for hydrogenation of aromatics, *ACS Catal.* 7 (2017) 5987–5991, <https://doi.org/10.1021/acs.catal.7b01816>.
- [25] Z. Zhang, Y. Zhu, H. Asakura, B. Zhang, J. Zhang, M. Zhou, Y. Han, T. Tanaka, A. Wang, T. Zhang, N. Yan, Thermally stable single atom Pt/m-Al₂O₃ for selective hydrogenation and CO oxidation, *Nat. Commun.* 8 (2017) 16100, <https://doi.org/10.1038/ncomms16100>.
- [26] Y. Zhao, L. Wang, A. Kochubei, W. Yang, H. Xu, Y. Luo, A. Baiker, J. Huang, Z. Wang, Y. Jiang, Formation and location of Pt single sites induced by pentacoordinated Al species on amorphous silica-alumina, *J. Phys. Chem. Lett.* 12 (2021) 2536–2546, <https://doi.org/10.1021/acs.jpclett.1c00139>.
- [27] P. Geng, L. Wang, M. Du, Y. Bai, W. Li, Y. Liu, S. Chen, P. Braunstein, Q. Xu, H. Pang, MIL-96-Al for Li-S battery: shape or size? *Adv. Mater.* 34 (2022) 2107836, <https://doi.org/10.1002/adma.202107836>.
- [28] Q. Li, Z.H. Yue, Y.L. Li, Y.J. Hao, X.J. Wang, R. Su, F.T. Li, Construction of dual-defective Al₂O₃/Bi_{1.2}O_{1.2}Cl₂ heterojunctions for enhanced photocatalytic molecular oxygen activation via defect coupling and charge separation, *Ind. Eng. Chem. Res.* 61 (2021) 441–452, <https://doi.org/10.1021/acs.iecr.1c04440>.
- [29] G. Kresse, J. Furthmüller, Efficient iterative schemes for ab initio total-energy calculations using a plane-wave basis set, *Phys. Rev. B* 54 (1996) 11169, <https://doi.org/10.1103/PhysRevB.54.11169>.
- [30] G. Kresse, J. Hafner, Ab initio molecular-dynamics simulation of the liquid-metal-amorphous-semiconductor transition in germanium, *Phys. Rev. B* 49 (1994) 14251–14269, <https://doi.org/10.1103/PhysRevB.49.14251>.
- [31] S. Grimme, J. Antony, S. Ehrlich, H. Krieg, A consistent and accurate ab initio parametrization of density functional dispersion correction (DFT-D) for the 94 elements H–Pu, *J. Phys. Chem. Lett.* 132 (2010) 154104, <https://doi.org/10.1063/1.3382344>.
- [32] J.P. Perdew, J.A. Chevary, S.H. Vosko, K.A. Jackson, M.R. Pederson, D.J. Singh, C. Fiolhais, Erratum: Atoms, molecules, solids, and surfaces: applications of the generalized gradient approximation for exchange and correlation, *Phys. Rev. B* 46 (1993) 6671–6687, <https://doi.org/10.1103/PhysRevB.48.4978.2>.
- [33] J.P. Perdew, K. Burke, M. Ernzerhof, Generalized gradient approximation made simple, *Phys. Rev. Lett.* 77 (1996) 3865–3868, <https://doi.org/10.1103/PhysRevLett.77.3865>.
- [34] B.W. Lee, R.F. Sawyer, Regge poles and high-energy limits in field theory, *Phys. Rev.* 127 (1962) 2266–2273, <https://doi.org/10.1103/PhysRev.127.2266>.
- [35] H. Sun, H.Q. Yin, W. Shi, W.L.L. Yang, X.W. Guo, H. Lin, J. Zhang, T.B. Lu, Z. M. Zhang, Porous β-FeOOH nanotube stabilizing Au single atom for high-efficiency nitrogen fixation, *Nano Res.* 15 (2022) 3026–3033, <https://doi.org/10.1007/s12274-021-3937-3>.
- [36] Z. Wang, Y. Jiang, O. Lafon, J. Trebosc, K. Duk Kim, C. Stampfl, A. Baiker, J. P. Amoureaux, J. Huang, Bronsted acid sites based on penta-coordinated aluminum species, *Nat. Commun.* 7 (2016) 13820, <https://doi.org/10.1038/ncomms13820>.
- [37] W. Liu, S. Yang, Q. Zhang, T. He, Y. Luo, J. Tao, D. Wu, H. Peng, Insights into flower-like Al₂O₃ spheres with rich unsaturated pentacoordinate Al³⁺ sites stabilizing Ru-CeO₂ for propane total oxidation, *Appl. Catal. B Environ.* 292 (2021) 120171, <https://doi.org/10.1016/j.apcatb.2021.120171>.
- [38] A. Düvel, E. Romanova, M. Sharifi, D. Freude, M. Wark, P. Heijmans, M. Wilkering, Mechanically induced phase transformation of γ-Al₂O₃ into α-Al₂O₃. Access to structurally disordered γ-Al₂O₃ with a controllable amount of pentacoordinated Al sites, *J. Phys. Chem. C* 115 (2011) 22770–22780, <https://doi.org/10.1021/jp206077r>.
- [39] Q. Zhang, P. Yang, H. Zhang, J. Zhao, H. Shi, Y. Huang, H. Yang, Oxygen vacancies in Co₃O₄ promote CO₂ photoreduction, *Appl. Catal. B Environ.* 300 (2022) 120729, <https://doi.org/10.1016/j.apcatb.2021.120729>.
- [40] Y. Dai, B. Liu, Z. Zhang, P. Guo, C. Liu, Y. Zhang, L. Zhao, Z. Wang, Tailoring the d-orbital splitting manner of single atomic sites for enhanced oxygen reduction, *Adv. Mater.* 35 (2023) 2210757, <https://doi.org/10.1002/adma.202210757>.
- [41] Y.Y. Li, Y. Liu, H.Y. Mu, R.H. Liu, Y.J. Hao, X.J. Wang, X. Liu, D. Hildebrandt, F. T. Li, The simultaneous adsorption, activation and in situ reduction of carbon dioxide over Au-loading BiOCl with rich oxygen vacancies, *Nanoscale* 13 (2021) 2585–2592, <https://pubs.rsc.org/en/content/articlelanding/2021/nr/d0nr08314c>.
- [42] G. Xiang, S. Zhao, C. Wei, C. Liu, H. Fei, Z. Liu, S. Yin, Atomically dispersed Au catalysts for preferential oxidation of CO in H₂-rich stream 296 (2021) 120385, <https://doi.org/10.1016/j.apcatb.2021.120385>.
- [43] Z. Zhao, D. Xiao, K. Chen, R. Wang, L. Liang, Z. Liu, I. Hung, Z. Gan, G. Hou, Nature of five-coordinated Al in γ-Al₂O₃ revealed by ultra-high field solid-state NMR, *ACS Cent. Sci.* 8 (2022) 795–803, <https://doi.org/10.1021/acscentsci.1c01497>.
- [44] K. Yan, B. Gao, X. Zheng, M. Cheng, N. Zhou, X. Liu, L. Du, F. Yuan, J. Wang, X. Cui, G. Zhang, W. Kong, Q. Xu, Cooperatively tailored surface frustrated Lewis pairs and N-doping on CeO₂ for photocatalytic CO₂ reduction to high-value hydrocarbon products, *Appl. Catal. B Environ.* 343 (2024) 123484, <https://doi.org/10.1016/j.apcatb.2023.123484>.
- [45] J. Sun, J. Bian, J. Li, Z. Zhang, Z. Li, Y. Qu, L. Bai, Z.D. Yang, L. Jing, Efficiently photocatalytic conversion of CO₂ on ultrathin metal phthalocyanine/g-C₃N₄ heterojunctions by promoting charge transfer and CO₂ activation, *Appl. Catal. B Environ.* 277 (2020) 119199, <https://doi.org/10.1016/j.apcatb.2020.119199>.
- [46] G. Li, Y. Sun, Q. Zhang, Z. Gao, W. Sun, X. Zhou, Ag quantum dots modified hierarchically porous and defective TiO₂ nanoparticles for improved photocatalytic CO₂ reduction, *Chem. Eng. J.* 410 (2021) 128397, <https://doi.org/10.1016/j.cej.2020.128397>.
- [47] X. Jin, C. Lv, X. Zhou, H. Xie, S. Sun, Y. Liu, Q. Meng, G. Chen, A bismuth rich hollow Bi₄O₅Br₂ photocatalyst enables dramatic CO₂ reduction activity, *Nano Energy* 64 (2019) 103955, <https://doi.org/10.1016/j.nanoen.2019.103955>.
- [48] Z. Lin, Y. Wang, Z. Peng, Y.C. Huang, F. Meng, J.L. Chen, C.L. Dong, Q. Zhang, R. Wang, D. Zhao, J. Chen, L. Gu, S. Shen, Single-metal atoms and ultra-small clusters manipulating charge carrier migration in polymeric perylene diimide for efficient photocatalytic oxygen production, *Adv. Energy Mater.* 12 (2022) 2200716, <https://doi.org/10.1002/aenm.202200716>.
- [49] X. Qian, B. Li, H.Y. Mu, J. Ren, Y. Liu, Y.J. Hao, F.T. Li, Deep insight into the photocatalytic activity and electronic structure of amorphous earth-abundant MgAl₂O₄, *Inorg. Chem. Front.* 4 (2017) 1832–1840, <https://doi.org/10.1039/C7QI00478H>.
- [50] L. Jing, X. Sun, B. Xin, B. Wang, W. Cai, H. Fu, The preparation and characterization of La doped TiO₂ nanoparticles and their photocatalytic activity, *J. Solid. State Chem.* 177 (2004) 3375–3382, <https://doi.org/10.1016/j.jssc.2004.05.064>.
- [51] N. Wu, J. Wang, D.N. Tafen, H. Wang, J.G. Zheng, J.P. Lewis, X. Liu, S.S. Leonard, A. Manivannan, Shape-enhanced photocatalytic activity of single-crystalline anatase TiO₂ (101) nanobelts, *J. Am. Chem. Soc.* 132 (2010) 6679–6685, <https://doi.org/10.1021/ja909456f>.
- [52] S. Gong, G. Zhu, R. Wang, F. Rao, X. Shi, J. Gao, Y. Huang, C. He, M. Hojamberdiev, Synergistically boosting highly selective CO₂ to CO photoreduction over BiOCl nanosheets via in-situ formation of surface defects and non-precious metal nanoparticles, *Appl. Catal. B Environ.* 297 (2021) 120413, <https://doi.org/10.1016/j.apcatb.2021.120413>.
- [53] N. Ulagappan, H. Frei, Mechanistic study of CO₂ photoreduction in Ti silicalite molecular sieve by FT-IR spectroscopy, *J. Phys. Chem. A* 104 (2000) 7834–7839, <https://doi.org/10.1021/jp001470i>.

- [54] T. Wang, X. Meng, P. Li, S. Ouyang, K. Chang, G. Liu, Z. Mei, J. Ye, Photoreduction of CO₂ over the well-crystallized ordered mesoporous TiO₂ with the confined space effect, *Nano Energy* 9 (2014) 50–60, <https://doi.org/10.1016/j.nanoen.2014.06.027>.
- [55] M. Ma, J. Chen, Z. Huang, W. Fa, F. Wang, Y. Cao, Y. Yang, Z. Rao, R. Wang, R. Zhang, Y. Zou, Y. Zhou, Intermolecular hydrogen bond modulating the selective coupling of protons and CO₂ to CH₄ over nitrogen-doped carbon layers modified cobalt, *Chem. Eng. J.* 444 (2022) 136585, <https://doi.org/10.1016/j.cej.2022.136585>.
- [56] J. Jiang, X. Wang, Q. Xu, Z. Mei, L. Duan, H. Guo, Understanding dual-vacancy heterojunction for boosting photocatalytic CO₂ reduction with highly selective conversion to CH₄, *Appl. Catal. B Environ.* 316 (2022) 121679, <https://doi.org/10.1016/j.apcatb.2022.121679>.
- [57] Z. Tang, W. He, Y. Wang, Y. Wei, X. Yu, J. Xiong, X. Wang, X. Zhang, Z. Zhao, J. Liu, Ternary heterojunction in rGO-coated Ag/Cu₂O catalysts for boosting selective photocatalytic CO₂ reduction into CH₄, *Appl. Catal. B Environ.* 311 (2022) 121371, <https://doi.org/10.1016/j.apcatb.2022.121371>.
- [58] G. Pezzotti, W. Zhu, N. Sugano, E. Marin, K. Yamamoto, N. Nishiike, T. Hori, A. Rondinella, B.J. McEntire, R. Bock, B. Sonny Bal, Oxide ceramic femoral heads contribute to the oxidation of polyethylene liners in artificial hip joints, *J. Mech. Behav. Biomed.* 82 (2018) 168–182, <https://doi.org/10.1016/j.jmbbm.2018.03.021>.
- [59] Y. Chen, F. Wang, Y. Gao, F. Zhang, Y. Zou, Z. Huang, L. Ye, Y. Zhou, Interfacial oxygen vacancy engineered two-dimensional g-C₃N₄/BiOCl heterostructures with boosted photocatalytic conversion of CO₂, *ACS Appl. Energy Mater.* 3 (2020) 4610–4618, <https://doi.org/10.1021/acsaelm.0c00273>.
- [60] Y. Shi, G. Zhan, H. Li, X. Wang, X. Liu, L. Shi, K. Wei, C. Ling, Z. Li, H. Wang, C. Mao, X. Liu, L. Zhang, Simultaneous manipulation of bulk excitons and surface defects for ultrastable and highly selective CO₂ photoreduction, *Adv. Mater.* 33 (2021) 2100143, <https://doi.org/10.1002/adma.202100143>.
- [61] Z. Fan, W. Zhou, X. Qiu, H. Li, Y. Jiang, Z. Sun, D. Han, L. Niu, Z. Tang, Selective photocatalytic oxidation of methane by quantum-sized bismuth vanadate, *Nat. Sustain.* 4 (2021) 509–515, <https://doi.org/10.1038/s41893-021-00682-x>.